

Rainfall Climate Regimes: The Relationship of Regional TRMM Rainfall Biases to the Environment

WESLEY BERG, TRISTAN L'ECUYER, AND CHRISTIAN KUMMEROW

Department of Atmospheric Science, Colorado State University, Fort Collins, Colorado

(Manuscript received 3 January 2005, in final form 29 June 2005)

ABSTRACT

Intercomparisons of satellite rainfall products have historically focused on the issue of global mean biases. Regional and temporal variations in these biases, however, are equally important for many climate applications. This has led to a critical examination of rainfall estimates from the Tropical Rainfall Measuring Mission (TRMM) Microwave Imager (TMI) and precipitation radar (PR). Because of the time-dependent nature of these biases, it is not possible to apply corrections based on regionally defined characteristics. Instead, this paper seeks to relate PR–TMI differences to physical variables that can lead to a better understanding of the mechanisms responsible for the observed differences. To simplify the analysis, issues related to differences in rainfall detection and intensity are investigated separately. For clouds identified as raining by both sensors, differences in rainfall intensity are found to be highly correlated with column water vapor. Adjusting either TMI or PR rain rates based on this simple relationship, which is relatively invariant over both seasonal and interannual time scales, results in a 65%–75% reduction in the rms difference between seasonally averaged climate rainfall estimates. Differences in rainfall detection are most prominent along the midlatitude storm tracks, where widespread, isolated convection trailing frontal systems is often detected only by the higher-resolution PR. Conversely, over the East China Sea clouds below the ~ 18 -dBZ PR rainfall detection threshold are frequently identified as raining by the TMI. Calculations based on in situ aerosol data collected south of Japan support a hypothesis that high concentrations of sulfate aerosols may contribute to abnormally high liquid water contents within nonprecipitating clouds in this region.

1. Introduction

Recent advances in sensor technology, most notably related to the launch of the Tropical Rainfall Measuring Mission (TRMM) in late 1997, along with improvements in algorithm formulations have led to significantly better and more consistent rainfall estimates over the globe. The occurrence of an intense El Niño event in late 1997 and early 1998 provided an opportunity to observe the response of tropical precipitation to ENSO using data from TRMM. Figure 1 shows a comparison of tropical mean rainfall from version 5 of the TRMM Microwave Imager (TMI) 2A12 (Kummerow et al. 2001) and precipitation radar (PR) 2A25 (Iguchi et al. 2000) standard rainfall products over both land (Fig. 1a) and ocean (Fig. 1b) regions. Over land, the

two estimates show remarkably good agreement, even though the TMI retrieval relies on a less physically direct scattering-based retrieval, which relates 85-GHz brightness temperature depressions associated with frozen hydrometeors to surface rainfall (Kummerow et al. 2001). Over ocean regions, however, the TMI estimates in Fig. 1b show a significant increase in tropical mean oceanic rainfall during the 1997/98 El Niño while the PR estimates exhibit little or no response. Unfortunately, the lack of realistic and verifiable error estimates makes it impossible to determine if either the response indicated by the TMI estimates or the lack of response in the PR estimates is real or an artifact of the retrievals. Interestingly, as shown in Fig. 1c, there is excellent agreement between passive microwave rainfall estimates from various TMI and Special Sensor Microwave Imager (SSM/I) retrieval algorithms. This suggests that the discrepancy in the response of the TMI–PR estimates to ENSO is the result of fundamental physical differences and is not because of differences in sampling and/or algorithm formulation.

Corresponding author address: Wesley Berg, Dept. of Atmospheric Science, Colorado State University, Fort Collins, CO 80523-1371.

E-mail: berg@atmos.colostate.edu

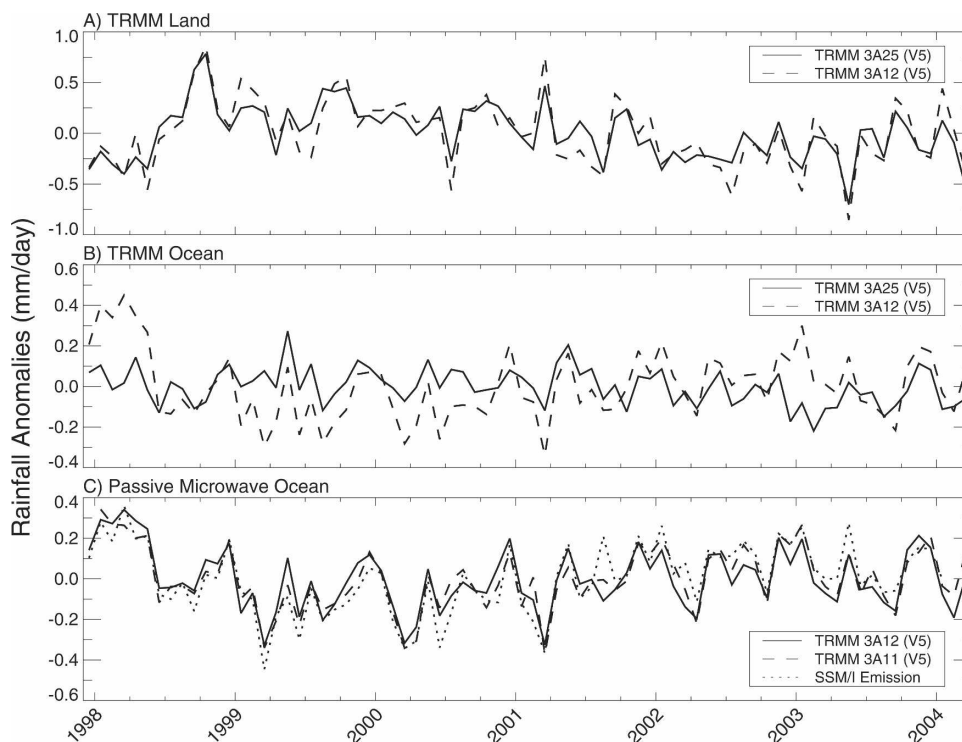


FIG. 1. Time series of tropical mean rainfall anomalies (30°N – 30°S) from the TRMM PR 3A25 and TMI 3A12 rainfall products over (a) land and (b) ocean. The 3A12 and 3A25 products are simply monthly accumulations of the instantaneous overpass estimates from the 2A12 and 2A25 retrieval algorithms. (c) A comparison of passive microwave estimates from TRMM (3A12 and 3A11) and SSM/I (Wilheit et al. 1991).

Previous work by Berg et al. (2002) found that discrepancies between satellite rainfall estimates averaged over large spatial and temporal domains for climate applications, like the one shown in Fig. 1, are the result of time-dependent regional biases. Differences in 5-yr mean rainfall from version 5 of the TMI 2A12 and PR 2A25 standard products are shown in Fig. 2. The tropical mean difference has been removed to emphasize the magnitude of the regional differences because the TMI 2A12 version 5 estimates exceed those from the PR 2A25 by approximately 24% over the tropical oceans and 20% over tropical land regions (Kummerow et al. 2001). Regionally, the TMI estimates show the largest bias relative to the PR over the central/east Pacific Ocean ITCZ, while the PR estimates exceed those from the TMI by the largest margin over the area just east of Australia in the subtropical south Pacific. Scatterplots for three selected $10^{\circ} \times 10^{\circ}$ regions roughly corresponding to previous field experiments over tropical ocean regions are also shown in Fig. 2. In all three cases the individual points, which correspond to 1° latitude \times 1° longitude bins averaged over the entire 5-yr period, have correlations between 0.97 and 0.98. This indicates that the random errors have been reduced to a

very small level by averaging over such a long time period. Regional biases remain, however, with the ratio of the TMI to PR rain estimates varying from 1.08 over Kwajalein, Republic of the Marshall Islands, to 1.19 in the east Pacific and 0.97 in the Atlantic.

Both the temporal and regional rainfall biases shown in Figs. 1 and 2 are the result of systematic changes in precipitation systems associated with meteorological regimes (Berg et al. 2002). Because satellite rainfall retrieval algorithms are fundamentally underconstrained, a number of assumptions must be made in the retrieval. In other words, it is necessary to assume some mean value for parameters that are not directly measured by the satellite. Variations in these parameters between meteorological regimes from the assumed values will result in regional/temporal biases in the rainfall estimates as shown in Figs. 1 and 2. The assumptions made by passive microwave retrievals (e.g., TMI) include the height of the water column, the shape of the vertical profile, the amount of cloud water (i.e., nonprecipitating drops), the shape and density of ice particles, the relationship of liquid water content to rain rate, and horizontal inhomogeneity within the sensor field of view. The PR retrievals must assume values for sub-

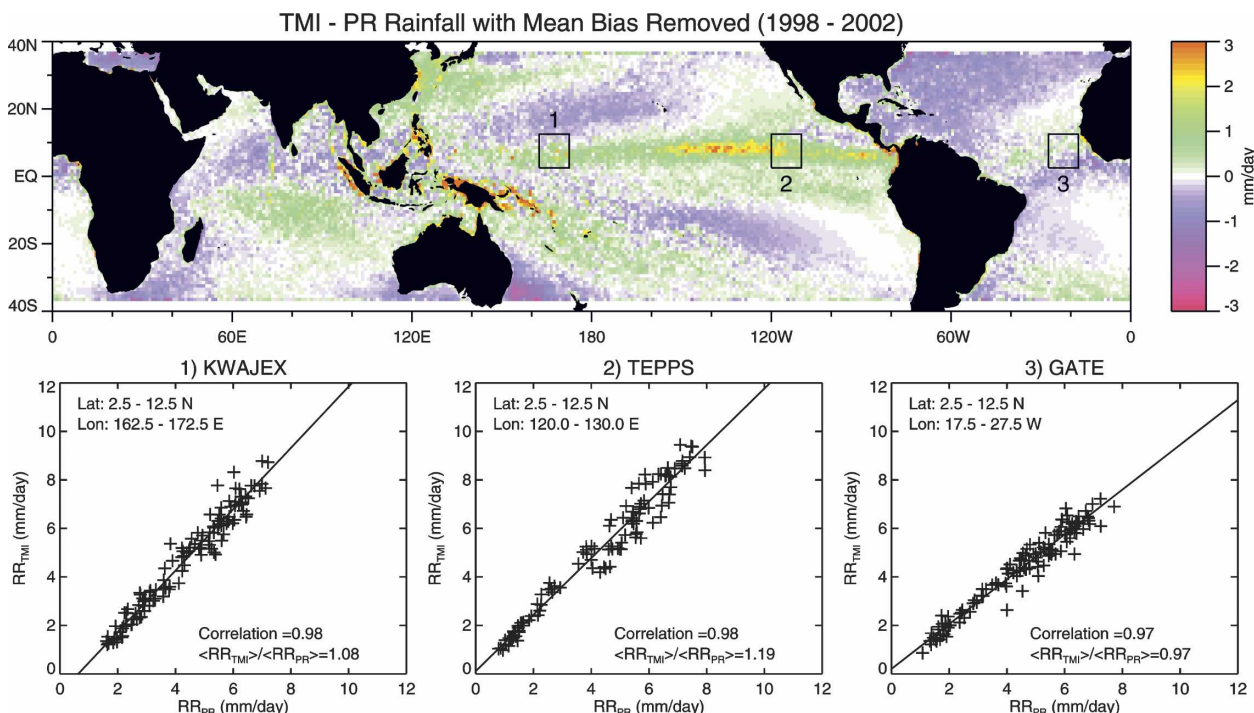


FIG. 2. (top) Rainfall difference map between version 5 of the TRMM TMI (2A12) and PR (2A25) retrieval algorithms for the 5-yr period from 1998 through 2002. The mean bias has been removed to emphasize regional differences. The difference map was created from the 3G68 dataset, which matches the instantaneous TMI and PR estimates on a $0.5^\circ \times 0.5^\circ$ grid. (bottom) Scatterplots of 5-yr mean values from the two sensors averaged over $1^\circ \times 1^\circ$ grid boxes for three regions corresponding to prior oceanic field programs. These include 1) the Kwajalein Experiment (KWAJEX) in the west Pacific, 2) the Tropical East Pacific Process Studies (TEPPS) in the east Pacific, and 3) the Global Atmospheric Research Program (GARP) Atlantic Tropical Experiment (GATE) in the tropical Atlantic.

pixel inhomogeneity as well as the drop size distribution (DSD), which impacts both the attenuation correction and the reflectivity-to-rain-rate ($Z-R$) relationship. Regional and temporal variations in these and other assumed parameters introduce errors that appear random from a global perspective but are perceived as systematic biases at a particular location (Fig. 2). Similarly, an artificial enhancement or reduction in the “observed” climate variability (Fig. 1) may result if temporal changes in these biases do not average out over the globe.

Recognizing the importance of this issue for climate rainfall applications, several researchers have examined the impact of various assumptions on the PR and TMI retrievals. Robertson et al. (2003) and Ikai and Nakamura (2003) investigated the impact of regional changes in DSD on the PR attenuation correction and $Z-R$ relationship. They found strong evidence of DSD-related regional biases and suggest that this is a serious issue for studies of interannual variability. Although TMI brightness temperatures are significantly less sensitive to changes in DSD, Masunaga et al. (2002) determined that DSD assumptions do impact the conversion

from liquid water content to rain rate. Fu and Liu (2001) showed regional variability in the shape of the rain profile. Harris et al. (2000), Berg et al. (2002), and Ikai and Nakamura (2003) found biases in the freezing-level estimates used in TMI retrievals, especially over midlatitude regions during winter. Bauer et al. (1999), Olson et al. (2001), and Battaglia et al. (2003) investigated the overestimation of stratiform rain by passive microwave retrievals because of increased emission by melting hydrometeors in the bright band. Kummerow et al. (2004) quantified the impact of changes in the spatial variability of rain within the satellite field of view using collocated PR observations. They found regional variations in the partial beam-filling correction leading to biases as large as 15% over the Indian Ocean but determined that the impact on the tropical mean rainfall was less than 2%.

While progress has been made in identifying many of the assumptions leading to climate regime biases, changes over space and time complicate efforts to quantify and/or remove them. Attempts to relate the characteristics of precipitation systems to specific physical mechanisms globally are limited by the observing

capabilities of TRMM and other spaceborne sensors (Nesbitt et al. 2000, 2004; Petersen and Rutledge 2001; Berg et al. 2002; Del Genio and Kovari 2002; Masunaga et al. 2005). Detailed observations from field experiments have been used to relate changes in convective structure to synoptic conditions (Chen et al. 1996; Rickenbach and Rutledge 1998; DeMott and Rutledge 1998a,b; Houze et al. 2000; Petersen et al. 2002, 2003), although it is unclear how to export these results to other regions/times. The common theme of these studies, however, is that there is a robust underlying relationship between the organization and vertical structure of convection and the synoptic environment. The spatial organization of precipitating systems, their vertical development, and the partitioning between convective and stratiform rainfall are all found to be strong functions of surface temperature, integrated water vapor, buoyancy, low-level shear, and convergence in the surrounding environment. Given that differences in the characteristics of rain systems lead to biases in the satellite products (Berg et al. 2002), our goal is to relate PR–TMI differences to physical variables that can lead to a better understanding of the mechanisms responsible for the observed differences. By identifying variables that can act as proxies for systematic differences between rainfall estimates from the two sensors we hope to eliminate the need to define rainfall climate regimes by regional and temporal boundaries.

2. Data

The data used in this analysis include TRMM rainfall estimates from version 5 of the TMI 2A12 (Kummerow et al. 2001) and the PR 2A25 (Iguchi et al. 2000) retrieval algorithms. The TRMM satellite is in a 350-km circular orbit with an inclination of 35° . To save fuel used in station-keeping operations and to prolong the life of the mission, the TRMM orbit was boosted to 402 km in August 2001. However, only data from the pre-boost period were used in the following analysis. The TMI is a nine-channel dual-polarized passive microwave radiometer with a swath width of 759 km and a nominal resolution of $30 \text{ km} \times 18 \text{ km}$ for the 19.35-GHz channels, which provide the primary liquid water emission information utilized in the ocean retrieval algorithm. The PR is the first and currently the only spaceborne precipitation radar. It has a swath width of 215 km, a nominal spatial resolution of 4.3 km at nadir, and a vertical resolution of 250 m. Detailed specifications for the TRMM spacecraft as well as the TMI and PR instruments are provided by Kummerow et al. (1998, 2000).

Because the retrieval techniques employed for the active (PR) and passive (TMI) TRMM sensors rely on

different physics, collocated estimates from these sensors are used to provide insights into the physical mechanisms leading to errors in the retrievals. Given that the spatial resolution of the TMI sensor is significantly lower than that of the PR, the PR rain estimates have been averaged over the 19-GHz footprint of the TMI using a Gaussian weighting scheme, which provides a close approximation to the TMI antenna pattern or field of view. Bennartz (1999) provides more details regarding using a Gaussian approximation to the radiometer antenna pattern. While there is some uncertainty in the matchups resulting from the different view angles between the sensors, this presumably random effect should average out over a large number of samples.

3. Differences in mean DJF 1999/2000 rainfall from PR and TMI

Pixel-level PR and TMI estimates were matched over a 3-month period from December 1999 through February 2000 (DJF 1999/2000). The estimates were matched at the pixel level to minimize the effect of averaging raining with nonraining pixels and/or multiple storm types. It was determined using $0.5^\circ \times 0.5^\circ$ gridded averages from the 3G68 dataset that even this level of pixel averaging significantly reduced the correlation between the rainfall biases and the selected proxy variables. To simplify the analysis we have chosen to separately address the issues of rainfall detection and rainfall intensity. The rainfall detection problem can be further divided into the case where the PR algorithm detects rain but the TMI does not, and the case where the TMI retrieval detects rain but the PR does not. For the case of light rain that is undetected by either sensor Schumacher and Houze (2000) used ground-based radar observations at the Kwajalein atoll in the west Pacific and found that the PR missed only 2.3% of near-surface rainfall, although it missed 46% of the near-surface rain area. While this may vary significantly from region to region, with the upcoming launch of CloudSat, which will fly a much more sensitive cloud radar, that issue should be better suited to be addressed (Stephens et al. 2002). The final case, and the one responsible for the most significant climate rainfall biases, occurs when both sensors detect rain, but provide disparate estimates of the intensity.

Figure 3 shows the relative magnitude for each of these bias sources during DJF 1999/2000. Note that the range of values for the differences in rainfall detection shown in Figs. 3e and 3f is one-half of that of the range shown in Figs. 3c and 3d. The relative difference between Figs. 3c and 3d indicates the impact of the differences in rainfall detection. While responsible for a

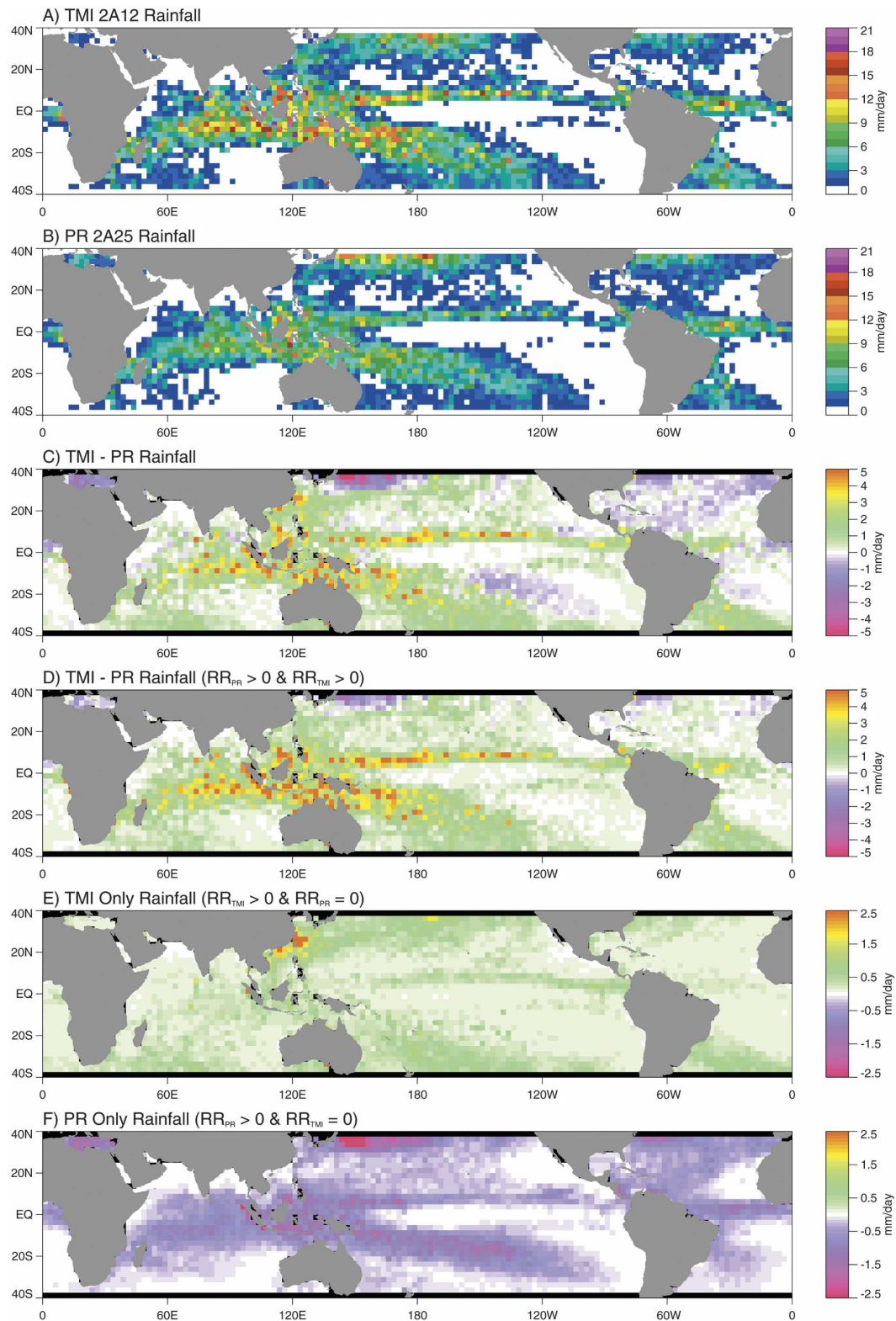


FIG. 3. Seasonal mean rainfall estimates from (a) TMI 2A12 and (b) PR 2A25 over the period from December 1999 through February 2000. The difference between the 2A12 and 2A25 estimates (c) using all of the collocated observations, and (d) including only those estimates for which both sensors detect rain. Rainfall threshold differences based on matched pixels indicating rainfall by (e) TMI and (f) PR only.

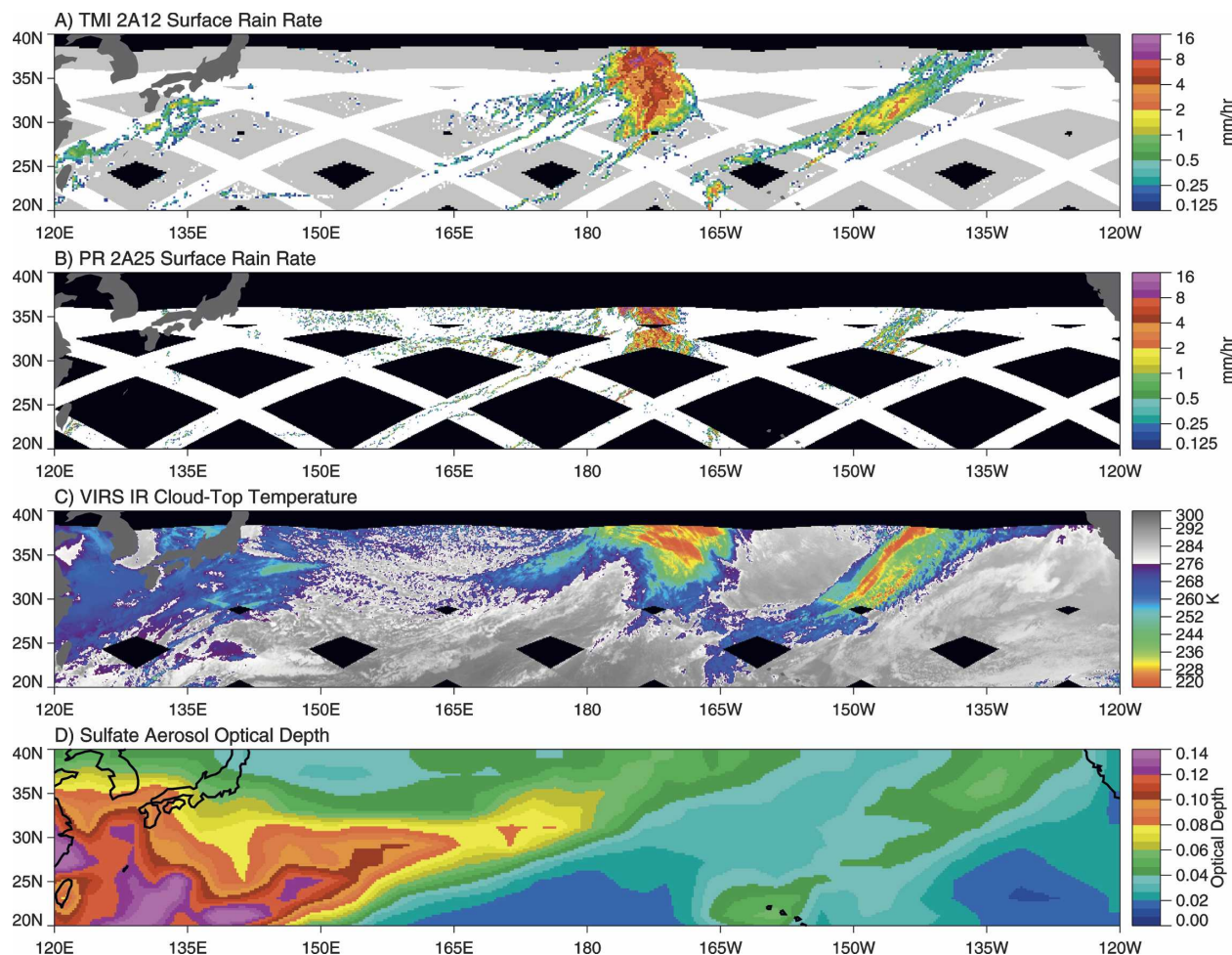


FIG. 4. (a) TMI 2A12 rainfall, (b) PR 2A25 rainfall, (c) VIRS cloud-top temperatures, and (d) model-derived sulfate aerosol optical depth for 1 Feb 2000. The nonraining portions of the TMI scan outside of the PR scan in (a) are gray; those nonraining TMI pixels within the PR scan are white.

relatively small fraction of the total climate rainfall difference over many regions, rainfall detection differences have a considerable impact over some regions. East of Japan there is a substantial amount of rain detected only by the PR, and over the East China Sea a sizable portion of the total climate rainfall difference is because of rain systems detected only by the TMI.

a. Rainfall detection (PR only)

The 17-dBZ threshold of the PR limits it to detecting rain rates greater than $0.2\text{--}0.4\text{ mm h}^{-1}$ over its $\sim 4\text{ km}$ field of view (Schumacher and Houze 2000). While the sensitivity of the TMI brightness temperatures is better than 1 K (Kummerow et al. 2000), the sensitivity of the retrieval algorithm is limited primarily by the difficulty of distinguishing precipitating from nonprecipitating clouds. Assuming a Marshall–Palmer (Marshall and Palmer 1948) drop size distribution, a cloud with

0.3 kg m^{-2} of cloud water, which roughly corresponds to the rain/no-rain threshold used in the TMI retrieval algorithm (Kummerow et al. 2001), would produce the same emission signal as that of a cloud with a 4-km freezing height raining at 0.8 mm h^{-1} . In addition, the relatively coarse resolution of the TMI ($\sim 25\text{ km}$) in comparison with that of the PR ($\sim 4\text{ km}$) means that over regions with frequently occurring isolated rain showers covering only a small portion of the TMI field of view, the TMI retrieval will necessarily underestimate rainfall because of its inability to resolve many of these events (Petty 1995, 1997). Figure 4 shows TMI and PR rain estimates over the northern subtropical Pacific along with the Visible and Infrared Scanner (VIRS) cloud-top temperature data for 1 February 2000. Although both sensors detect the intense rainfall associated with the frontal bands just east of the date line and at 140°W , the PR rain estimates indicate wide-

spread low-intensity rainfall behind the main system in the region north of 30°N between 150° and 180°E. The VIRS data confirm the presence of widespread patchy clouds over this region with relatively warm cloud tops. An examination of similar rain maps over the entire 3-month period indicates that this sort of weak isolated rainfall trailing eastward-propagating Pacific frontal bands occurs frequently poleward of 25°N. Of course, isolated rain cells occur across the globe resulting in a higher frequency of rain from the PR, but as Fig. 3f shows, during DJF 1999/2000 rainfall that escapes detection by the TMI accounts for a significantly higher percentage of the total rainfall in the midlatitude frontal regions than it does anywhere in the deep Tropics.

b. Rainfall detection (TMI only)

A widespread area of low-intensity rainfall identified by the TMI retrieval over the East China Sea, but not detected by the PR is also present in Fig. 4. Although the maximum TMI-estimated rain rates in this system are less than 4 mm h⁻¹, this corresponds to a significant amount of liquid water in the atmospheric column. Liquid water path (LWP) estimates from an optimal estimation retrieval algorithm indicate values exceeding 1 kg m⁻² in the areas of heaviest TMI-only rainfall. Because this is well above the effective threshold between cloud water and rain used by virtually all emission-based passive microwave retrieval algorithms, including the TMI 2A12, this feature would likely be retrieved as raining by any of these techniques. This would not be the case for scattering-based algorithms, however, because comparisons with raw TMI brightness temperatures (not shown) indicate a significant emission signal resulting from liquid hydrometeors but little or no scattering signal associated with frozen hydrometeors aloft. This is consistent with the VIRS infrared data shown in Fig. 4c, which indicate shallow clouds with the coldest cloud-top temperatures between 250 and 260 K.

A possible explanation for the absence of rainfall in the PR retrieval could be due, in part, to a modification of the size distribution of cloud droplets by aerosol particles along the lines of the second indirect aerosol effect proposed by Albrecht (1989). Indeed, aerosol optical depths (AOD) from the Georgia Tech/Goddard Global Ozone Chemistry Aerosol Radiation and Transport (GOCART) model (Chin et al. 2000a, 2000b), shown in Fig. 4d, indicate high concentrations of sulfate aerosols in this region. Furthermore, comparisons throughout the DJF 1999/2000 period indicate that the occurrence of TMI-only rainfall in this region generally corresponds to similarly high sulfate AODs. The high

frequency of occurrence of TMI-only rain systems in this region results in a substantial overestimate by the TMI retrieval relative to the PR, which is evident in Figs. 3c and 3e. Insights into the plausibility of this mechanism can be gleaned from the Kessler-type parameterizations that are often used to represent the autoconversion of cloud droplets to raindrops in global climate models (GCMs). Consider the analytical expression for the critical radius required for the formation of embryonic raindrops that was developed by Liu et al. (2004):

$$r_c = \left[\left(\frac{3}{4\pi} \right)^2 \frac{v^2}{\kappa} \beta_{\text{con}} \frac{N}{L^2} \right]^{1/6} \approx 4.09 \times 10^{-4} \beta_{\text{con}}^{1/6} \frac{N^{1/6}}{L^{1/3}}, \quad (1)$$

where N is the number concentration of cloud droplets (cm⁻³), L is the liquid water content (LWC; g m⁻³), and $\beta_{\text{con}} \approx 1.15 \times 10^{23} \text{ s}^{-1}$. Liu and Daum (2004) demonstrate that autoconversion occurs when the sixth-moment radius, given by

$$r_6 = \left(\frac{3}{4\pi\rho_w} \right)^{1/3} \alpha \left(\frac{L}{N} \right)^{1/3}, \quad (2)$$

where $\alpha = 1.12$ and ρ_w is the density of water, exceeds r_c . Equating Eqs. (1) and (2), it can be demonstrated that autoconversion should occur any time the number concentration of cloud droplets in a cloud is fewer than

$$N_c = 24.36^2 L^{4/3}. \quad (3)$$

The critical number concentration defined in Eq. (3) is plotted as a function of LWC in Fig. 5. Clouds with a number concentration below N_c are assumed to contain large enough droplets to induce sufficient collision and coalescence to produce the embryonic raindrops necessary for precipitation development. On the other hand, no rainfall development is expected in clouds containing a higher concentration of small droplets because of a reduction in both the frequency of collisions and the coalescence efficiency between such droplets. This is the fundamental principle underlying the second indirect aerosol effect—that increased concentrations of hygroscopic aerosols leading to corresponding increases in the number of cloud droplets may potentially suppress the formation of precipitation.

Although it is an approximation, N_c provides a rough guideline for estimating the maximum amount of liquid water that the atmosphere can hold in the form of clouds before the onset of precipitation. For reference, observations of cloud droplet concentrations in “clean”

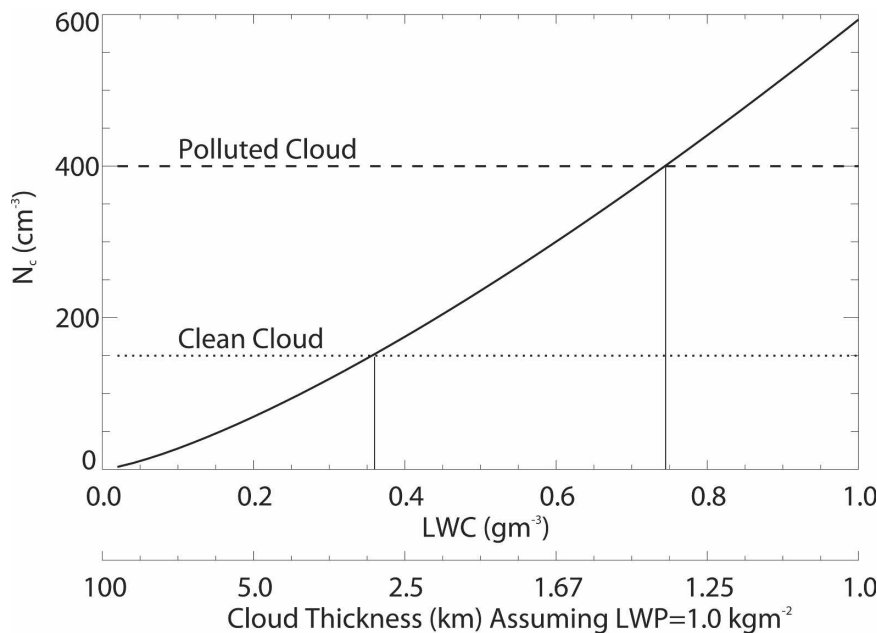


FIG. 5. Critical number concentration for the autoconversion of cloud droplets to precipitation using the Kessler-type parameterization of Liu and Daum (2004).

and “polluted” air masses obtained during the Asian Particle Environmental Change Studies (APEX) experiment that took place in the sea off the coast of Kyushu, Japan, in 2003 (Ishizaka et al. 2003) are illustrated in Fig. 5. The polluted air mass, characterized by 400 cloud droplets per cubic centimeter, can support approximately twice as much cloud water before precipitation is induced as can a clean air mass containing 150 droplets per cubic centimeter. In the rainfall scene in Fig. 4, TMI observations suggest that LWPs in the East China Sea region range from 0.5 to 1.2 kg m⁻². Such values are generally assumed to be indicative of rainfall, but Fig. 5 demonstrates that this is not necessarily the case in a polluted environment. In such a case, a 1.5-km-thick cloud with an LWP of 1 kg m⁻² may contain enough droplets to preclude the development of significant precipitation.

Because radar reflectivity is sensitive to drop size to the sixth power, the distinction between cloud droplets and raindrops is a critical factor governing the ability of the PR to detect liquid water. Suppose, for example, the PR encounters a pixel containing a 1.5-km-thick cloud with an LWP of 1 kg m⁻². Figure 6 illustrates two DSDs that could represent this cloud—one corresponding to the convective rainfall DSD assumed by the PR rainfall algorithm (Iguchi et al. 2000) and the other corresponding to a combination of cloud and drizzle droplets. The cloud and drizzle droplets are modeled as a sum of two lognormal distributions,

$$N(r) = \frac{N_{\text{cld}}}{\sigma_{\log, \text{cld}} r \sqrt{2\pi}} \exp \left[-\frac{\left(\ln \frac{r}{r_{g, \text{cld}}} \right)^2}{2\sigma_{\log, \text{cld}}^2} \right] + \frac{N_d}{\sigma_{\log, d} r \sqrt{2\pi}} \exp \left[-\frac{\left(\ln \frac{r}{r_{g, d}} \right)^2}{2\sigma_{\log, d}^2} \right], \quad (4)$$

with geometric mean radii $R_{g, \text{cld}} = 9 \mu\text{m}$ and $R_{g, d} = 50 \mu\text{m}$ and width parameters $\sigma_{\log, \text{cld}} = 0.5$ and $\sigma_{\log, d} = 0.35$, consistent with the drizzle observations of Frisch et al. (1995) and the liquid cloud climatology of Miles et al. (2000). The total number concentration of cloud drops (N_{cld}) is fixed at 400 cm⁻³, consistent with the observations of Ishizaka et al. (2003) for a polluted air mass, leaving ~15% of the total LWC to occur in the form of drizzle. This leads to a total number of drizzle drops $N_d = 0.7 \text{ cm}^{-3}$, which is in good agreement with the concentrations observed by Frisch et al. (1995).

For this case, the raindrop DSD yields a reflectivity of 40 dBZ while the cloud/drizzle distribution yields that of 18 dBZ. Using the Z – R relationship from the PR 2A25 retrieval, this corresponds to rainfall rates of 15 and 0.3 mm h⁻¹, respectively. In fact, because the minimum detectable signal of the PR is ~18 dBZ, it is possible that the combinations of cloud and drizzle would not be detected. The absence of rainfall in the PR estimates over the East China Sea in Fig. 4 can therefore

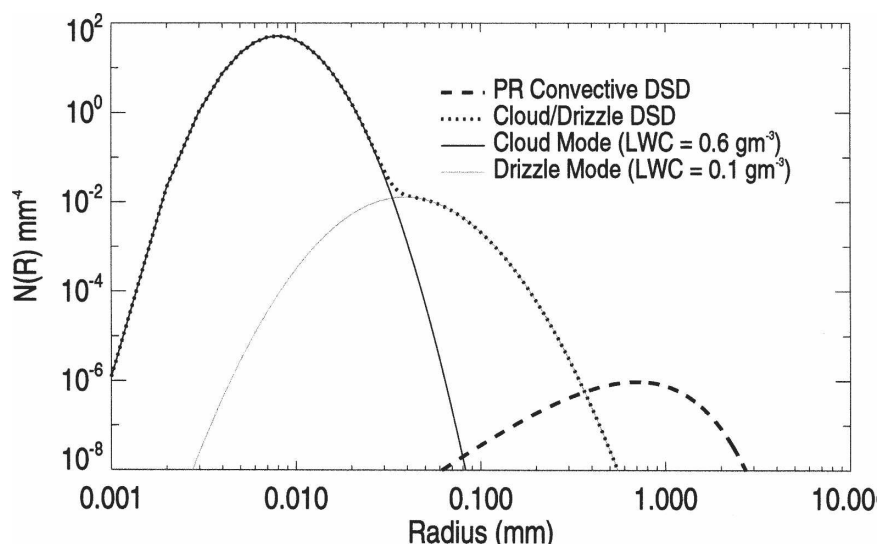


FIG. 6. Precipitation (dashed curve) and drizzle (dotted curve) DSDs, each with an LWC of 0.8 g m^{-3} .

be reconciled with the 1 kg m^{-2} LWP retrieved from collocated TMI observations if one adopts a DSD that might be expected in cases of heavy sulfate aerosol concentrations, as shown in Fig. 4d. These calculations should not, however, be interpreted as proof that rainfall suppression by aerosols is the sole factor responsible for nonzero TMI rainfall rates in the absence of any signal in the PR. Instead, they are meant to test the plausibility of such a mechanism, indicating that it could produce in principle the observed inconsistency between the TMI and PR rain estimates.

c. Rainfall intensity

The most significant climate rainfall biases occur when both sensors/algorithms detect rain, but they provide different estimates of the intensity. As shown in Fig. 3d, the impact of these differences in rainfall intensity can be substantial. Because of seasonal and interannual changes in the regional patterns, however, it is of little value to characterize these differences by region. Instead, our goal is to identify a globally observable physical variable that can be used as a proxy for the systematic differences between the TMI and PR rain estimates. A number of different variables were investigated, including sea surface temperature (SST); total column water vapor and surface wind speed observations from TMI (Wentz and Spencer 1998; Wentz et al. 2000); ocean surface wind speed and divergence estimates from the Quick Scatterometer (QuikScat); relative humidity at several levels from the National Centers for Environmental Prediction–National Center for Atmospheric Research (NCEP–NCAR) and the

European Centre for Medium-Range Weather Forecasts (ECMWF) reanalyses; AODs from the GOCART model; and storm system characteristics from PR observations within the TMI field of view, including storm height, brightband height, convective rain fraction, mean surface rain rate, mean surface reflectivity, and spatial inhomogeneity.

The specified variables were matched to instantaneous TRMM rain estimates at the TMI resolution. Variables such as SST and ocean surface wind speed, which cannot be retrieved for raining scenes, were interpolated from neighboring pixels. Column water vapor estimates are retrieved for pixels with rain rates below $\sim 15 \text{ mm h}^{-1}$ (Wentz and Spencer 1998) and are interpolated from neighboring pixels for more intense rain systems. Matched raining pixels for the entire 3-month period (~ 5.3 million) were divided into 30 categories based on the variable being analyzed, and mean values of the TMI/PR surface rainfall ratio were computed for each category. The pixel-level TMI rain estimates were then “adjusted” based on the mean rainfall ratio corresponding to the value of the collocated proxy variable. It should be noted that the purpose of this adjustment was not to correct for any climate biases because that would imply that the PR estimates were unbiased, but was instead to determine if the TMI–PR differences were correlated with a given proxy variable. To evaluate the impact of this adjustment, climate rainfall estimates were computed from both the original and adjusted TMI estimates over 1° latitude \times 1° longitude boxes for the entire 3-month period. While an adjustment based on many variables, including SST, re-

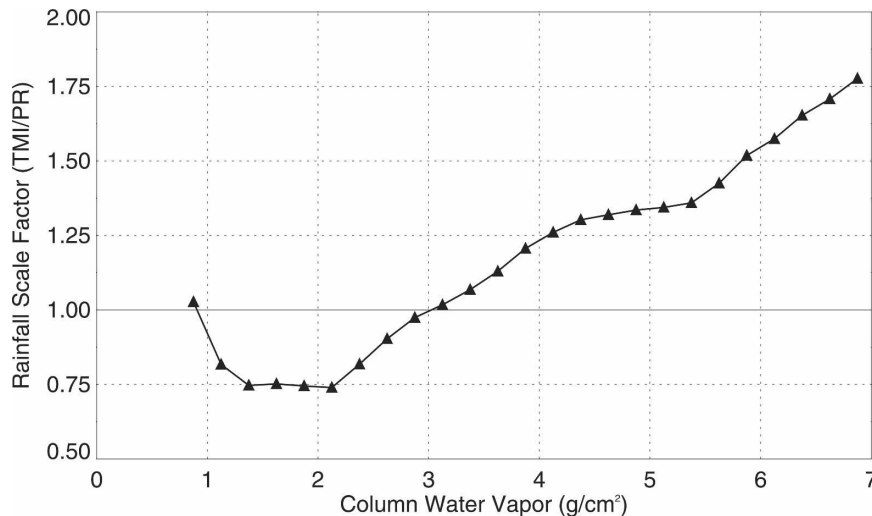


FIG. 7. The ratio of TMI to PR rain rate as a function of column water vapor for DJF 1999/2000.

sults in a significant decrease in the TMI–PR difference over certain regions, increases over other regions indicate a regional dependence in the relationship between the candidate proxy variable and the rainfall difference. The relationship of TMI–PR differences to column water vapor estimates, however, does not appear to vary significantly between regions. Figure 7 shows the mean TMI/PR rainfall ratio as a function of column water vapor. For low-water-vapor regions, which occur exclusively in midlatitude areas, the PR rain estimates exceed those from the TMI, while over moist, deep tropical regions the TMI estimates exceed those from the PR by almost a factor of 2.

Difference maps between the TMI and PR climate rainfall estimates are shown in Fig. 8 for the original and adjusted rainfall estimates based on the relationship with column water vapor shown in Fig. 7. Both the rainfall difference maps and scatterplots of the 3-month binned averages shown in Figs. 8c and 8d indicate a significant reduction in variance after the water vapor–based rainfall adjustment. The rms difference between the 3-month gridded estimates is reduced from 1.18 to 0.36, amounting to a nearly 70% reduction in the variance of the climate rainfall differences between the two sensors. Not all of the systematic regional differences are related to column water vapor because residual biases remain; however, the remaining differences are comparatively small.

4. Time-dependent variations

To evaluate the impact of seasonal and interannual changes on differences between the PR and TMI estimates, rainfall difference maps are shown in Fig. 9 for

six different 3-month periods. These six periods include the 1997/98 El Niño and subsequent La Niña, which extended from late 1998 through 2000, as well as the annual cycle between December 1999 and November 2000. The largest differences between TMI and PR are evident during DJF 1997/98, when El Niño conditions led to a substantial increase in rainfall across the central and east Pacific. Relative to the PR estimates, the overestimation of rainfall by the TMI is the largest and most widespread at this time, although the central/east Pacific ITCZ regularly exhibits sizable differences. Conversely, the PR estimates exceed those from the TMI in areas with minimal rainfall and in the midlatitudes, most notably over the Pacific during winter.

Figure 10 shows the impact of differences in rainfall detection between the two algorithms/sensors for all six seasons. The cases where only one of the two sensors/algorithms detect rain, as shown in Figs. 3e and 3f, have been combined with green/yellow/orange colors, indicating areas dominated by cases where rain is detected by TMI only, and blue/purple colors, indicating regions dominated by PR-only rain. The largest impact of PR-only rainfall is from persistent isolated rainfall occurring over midlatitude regions during winter, although this is also an issue throughout the tropical convergence zones. Differences resulting from cases where the TMI detects rain that the PR does not appear to primarily be an issue outside of the Tropics. The bull's-eye over the East China Sea that is evident during DJF 1999/2000 occurs during the other seasons as well, although it is most pronounced during DJF. Figure 11 shows mean seasonal AODs from the Moderate Resolution Imaging Spectroradiometer (MODIS) based on 4 yr of observa-

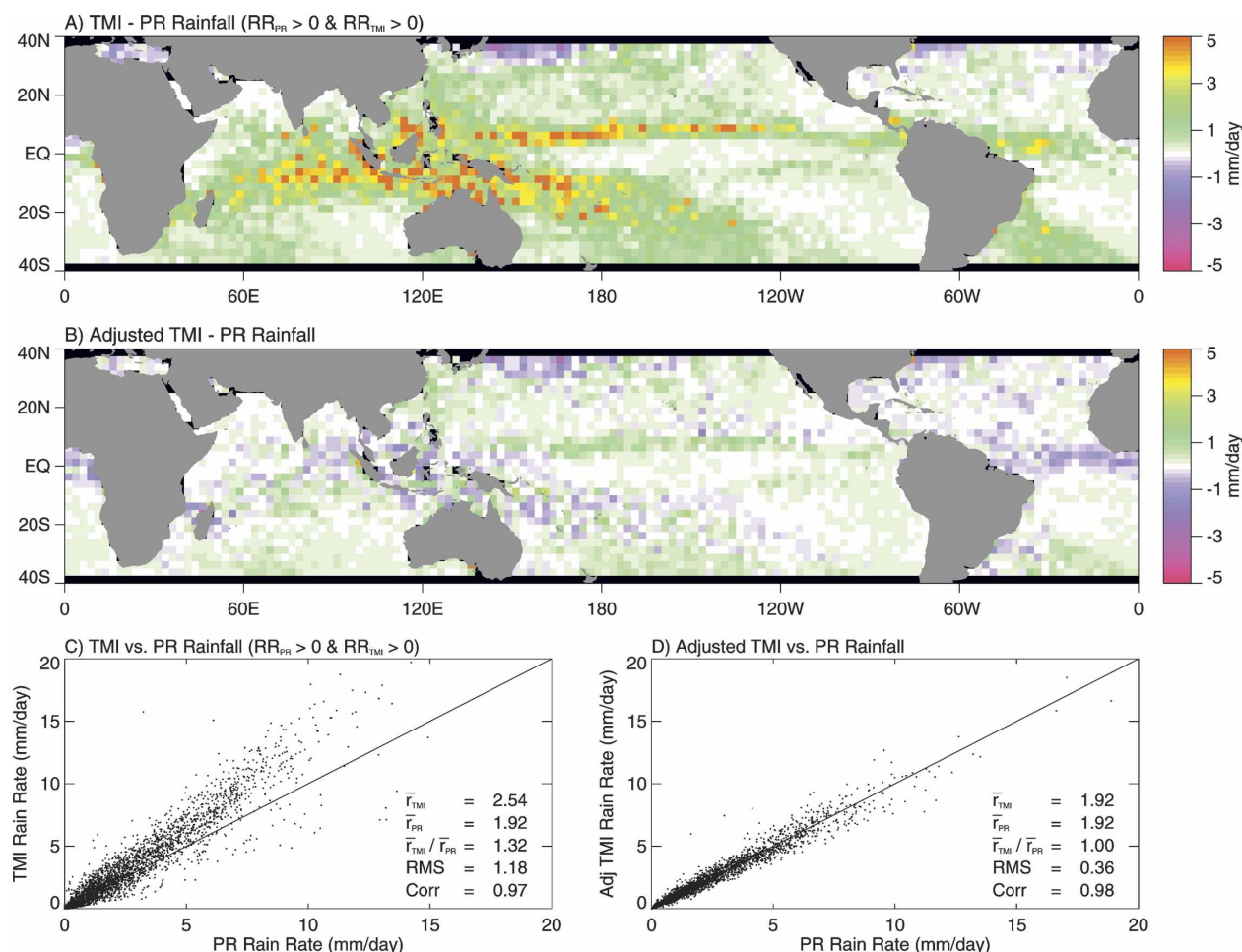


FIG. 8. The difference between seasonally averaged TMI 2A12 and PR 2A25 matched rainfall estimates for DJF 1999/2000 (a) before and (b) after the TMI rain estimates have been adjusted based on the column water vapor–categorized TMI/PR rainfall ratio. Scatterplots of the TMI vs PR rainfall estimates averaged over the 3-month period and 1° lat \times 1° lon boxes (c) before and (d) after the water vapor adjustment.

tions. While the period of the aerosol observations does not correspond directly to the periods shown in Fig. 10, high aerosol concentrations during DJF and March–May (MAM) over the East China Sea correspond with the frequent occurrence of TMI-only rainfall during those seasons. In addition, the eastward extent of TMI-only rainfall during MAM 2000 appears to correspond to particularly high AODs extending across the Pacific. While the apparent association between aerosols and rain threshold biases do not prove anything, it does advocate further study.

To determine whether the relationship between the TMI/PR rainfall ratio and column water vapor changes over time, the analysis described in section 3c was performed for all six seasons shown in Fig. 9. Figure 12 shows the relationship between the mean TMI/PR rain ratio and column water vapor for each period. Changes

in this relationship associated with the annual cycle are shown in Fig. 12a and changes resulting from interannual variability associated with El Niño are shown in Fig. 12b. While there appears to be both seasonal and interannual variations, the curves are remarkably consistent. To determine the significance of these differences, mean values of the TMI/PR rainfall ratio were computed from the entire 18-months of data as shown by the black curves in Fig. 12. This “universal” relationship was then used to adjust the TMI rain estimates for each of the six periods. Comparing the results shown in Fig. 13 with the original difference maps in Fig. 9, it is apparent that there is a substantial decrease in the variability of the climate rainfall differences across all seasons including DJF 1997/98. Residual differences remain, most notable in the Bay of Bengal during June–August (JJA) 2000, but the water vapor–based rainfall

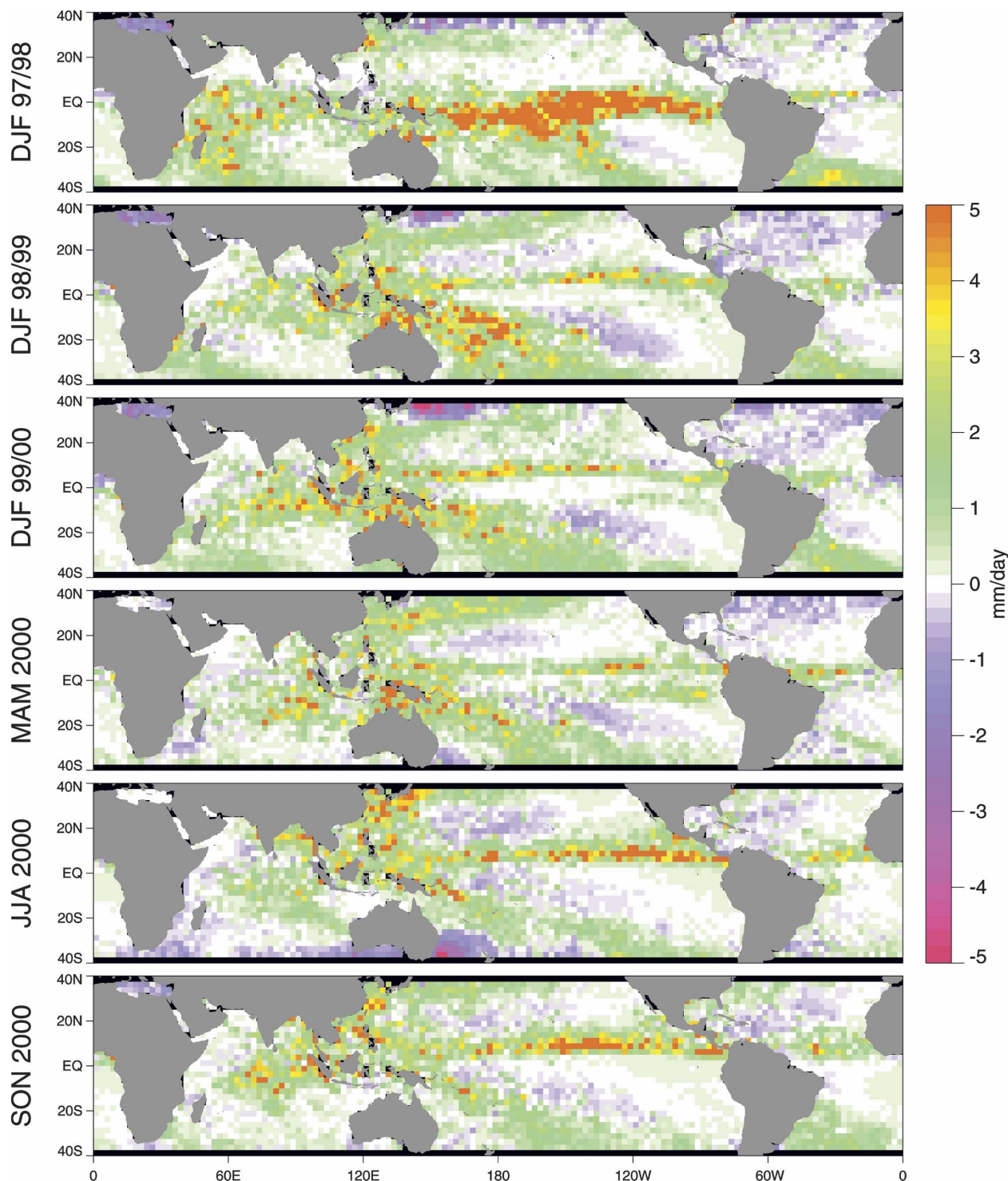


FIG. 9. Maps of the TMI - PR 3-month mean rainfall for the seasons of DJF 1997/98, DJF 1998/99, DJF 1999/2000, MAM 2000, JJA 2000, and SON 2000.

adjustment appears to be robust for both seasonal and interannual time scales.

Rms differences between the PR and TMI climate rainfall estimates are given in Table 1 for the original

and the adjusted values based on the universal (18 month) mean values. Results are given for the column water vapor-based rainfall adjustment, as well as similar adjustments using SST, surface wind speed, and

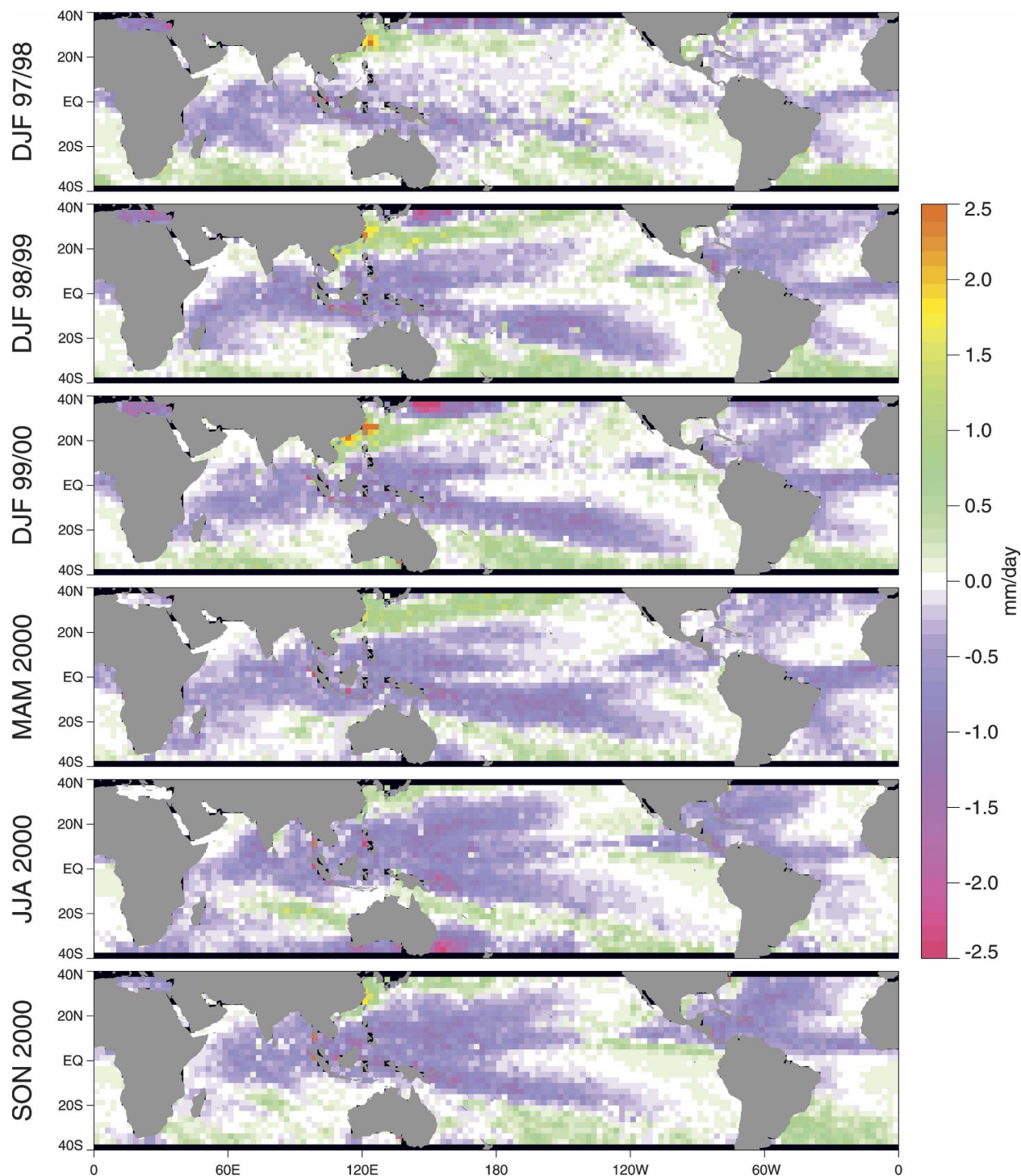


FIG. 10. Maps of the differences in rainfall detection for the seasons of (top to bottom) DJF 1997/98, DJF 1998/99, DJF 1999/2000, MAM 2000, JJA 2000, and SON 2000. Warm colors (green/yellow/orange) represent areas dominated by TMI-only rainfall while cool colors (blue/purple) highlight those dominated by PR-only rainfall.

both the PR and TMI rain rates. The water vapor-based rainfall adjustment consistently reduces the rms difference by 65%–75%. From Table 1 the rms of the water vapor-adjusted estimates was 0.38 for DJF 1999/

2000 using the universal adjustment, while this decreased to just 0.36 using the adjustment based on only the DJF 1999/2000 data. The other proxy variables show mixed success with a wind speed-based adjust-

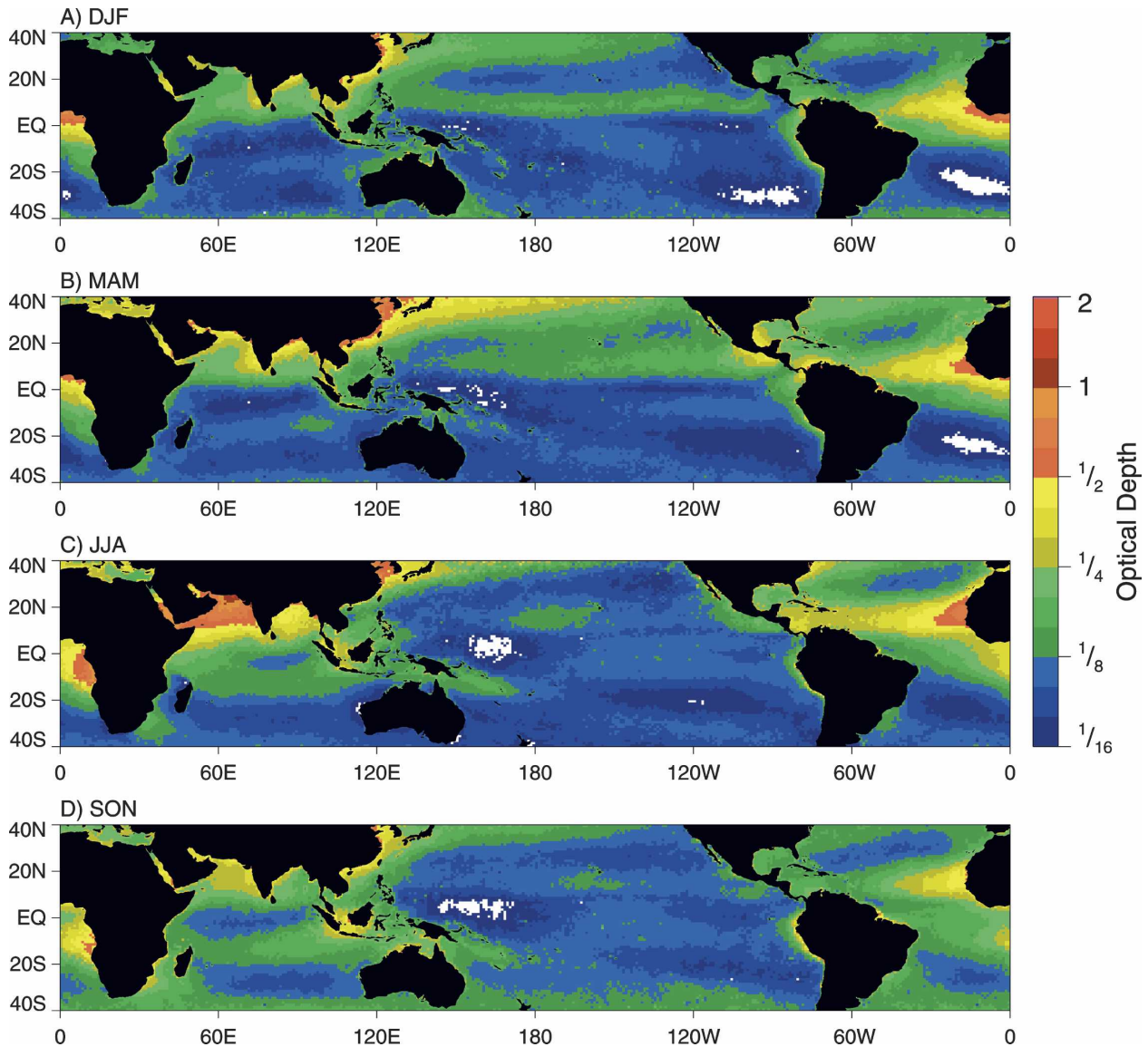


FIG. 11. Seasonal mean AODs from MODIS for the period from September 2000 through August 2004.

ment providing the next most significant improvement. An adjustment based on SST varies significantly between seasons, suggesting that the cloud properties that are associated with warmer SSTs in the central/east Pacific during the 1997/98 El Niño differ from the cloud properties over regions of warm SSTs during other years/seasons. Using rainfall intensity as a proxy for PR/TMI differences also leads to a significant reduction in the rms, which is independent of whether the TMI or PR rainfall estimates are used. For light rain events the TMI significantly overestimates relative to the PR, while for intense rain events the PR estimates exceed those from the TMI. None of these other proxy variables, however, produce as large a reduction in rms,

suggesting that column water vapor is most closely associated with regime-dependent structural and microphysical changes in rain systems, which lead in turn to biases in the TMI and PR rainfall estimates.

5. Algorithm assumptions leading to climate biases

As discussed in the summary of previous studies, a number of assumptions in both the TMI and PR retrieval algorithms may be responsible for the climate rainfall differences. Given the relationship of the TMI/PR differences with column water vapor, it is likely that many of the assumptions producing biases in the retrievals are correlated with water vapor. Observations

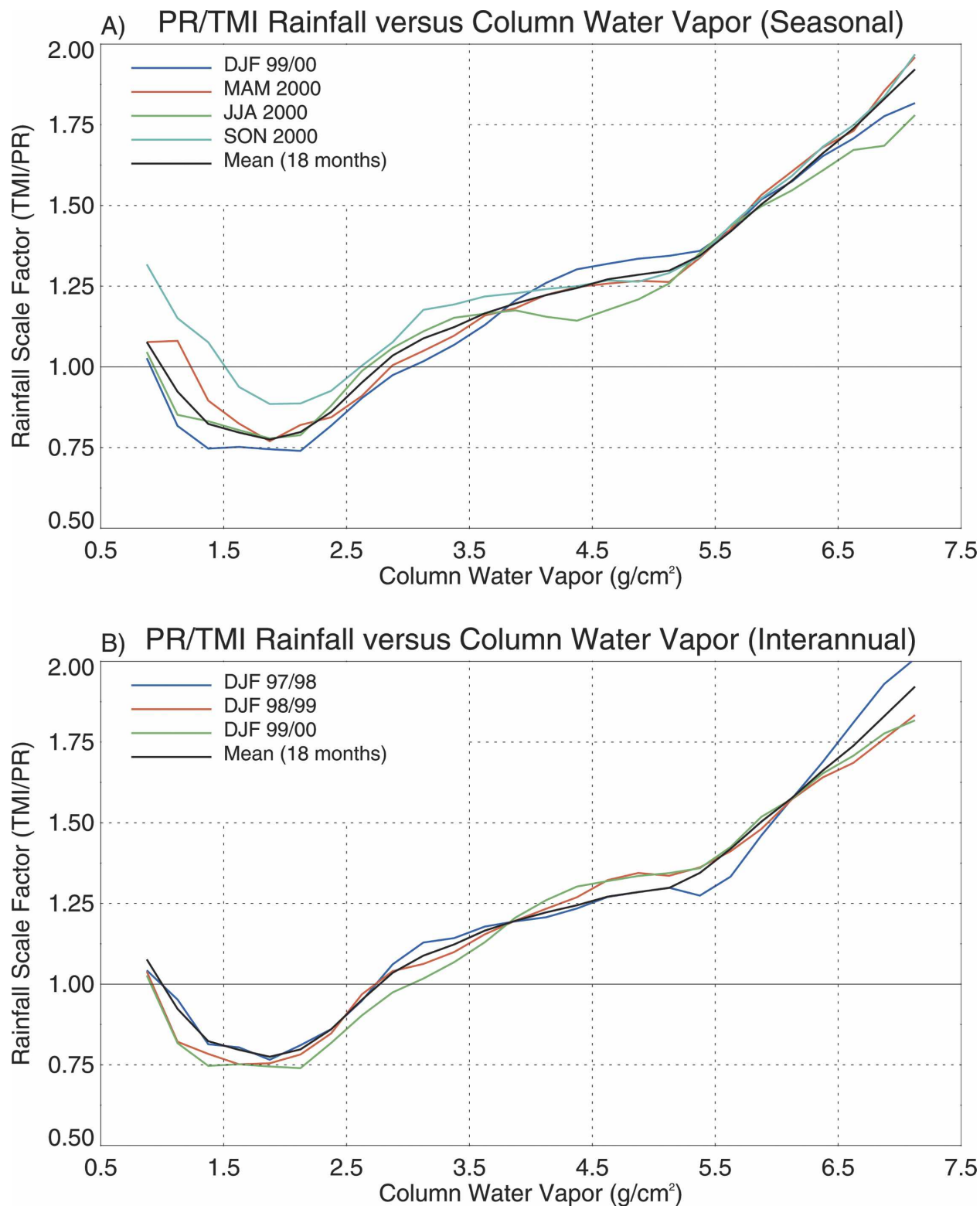


FIG. 12. The ratio of TMI to PR rain rate as a function of column water vapor for (a) DJF 1999/2000, MAM 2000, JJA 2000, and SON 2000, and (b) DJF 1997/98, DJF 1998/99, and DJF 1999/2000. The black line is the mean for all six periods/seasons (18 months).

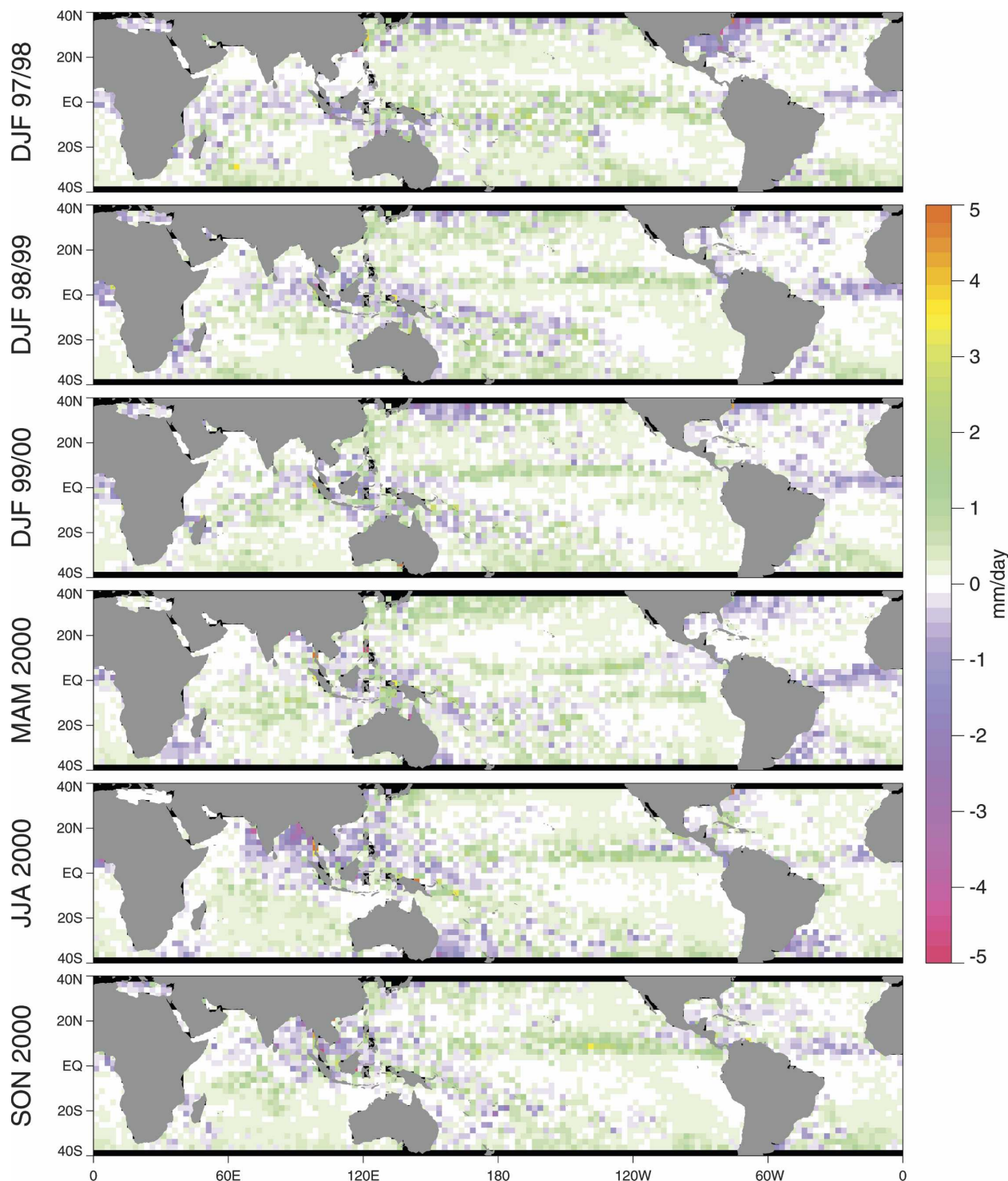


FIG. 13. Residual TMI - PR difference maps after the water vapor-based rainfall adjustment for the seasons of (top to bottom) DJF 1997/98, DJF 1998/99, DJF 1999/2000, MAM 2000, JJA 2000, and SON 2000.

from the PR can be used to investigate a number of TMI algorithm assumptions, including the freezing height, the shape of the rain profile, and rainfall inhomogeneity within the TMI field of view (Kummerow et

al. 2004). Figure 14 shows how two assumptions in the TMI retrieval—the height of the freezing level and the shape of the rain profile—vary as a function of column water vapor.

TABLE 1. Rms differences (mm day^{-1}) between TMI and PR rainfall estimates averaged over 3 months and $1^\circ \text{ lat} \times 1^\circ \text{ lon}$ boxes. The original values are the unmodified values; the other columns give the rms differences for the TMI rain estimates, which have been adjusted based on various proxy variables, including column water vapor, SST, ocean surface wind speed, TMI rainfall rate, and PR rainfall rate. The values in parentheses are the rms values for the adjusted TMI rain estimates as a percentage of the rms for the original TMI rain estimates.

Season	Original	Water vapor	SST	Wind speed	TMI rainfall rate	PR rainfall rate
DJF 1997/98	1.80	0.44 (25%)	0.74 (41%)	0.86 (48%)	1.10 (61%)	1.03 (57%)
DJF 1998/99	1.27	0.39 (31%)	1.02 (80%)	0.55 (44%)	0.72 (56%)	0.63 (50%)
DJF 1999/2000	1.18	0.38 (32%)	1.04 (88%)	0.60 (50%)	0.71 (59%)	0.64 (54%)
MAM 2000	1.16	0.38 (35%)	1.03 (94%)	0.50 (46%)	0.64 (59%)	0.56 (51%)
JJA 2000	1.28	0.42 (35%)	1.08 (89%)	0.58 (48%)	0.73 (60%)	0.64 (53%)
SON 2000	1.29	0.36 (30%)	1.01 (85%)	0.46 (38%)	0.69 (58%)	0.57 (48%)
Mean	1.33	0.40 (31%)	0.99 (76%)	0.59 (46%)	0.76 (59%)	0.68 (53%)

The 2A12 algorithm calculates an estimate of the freezing level using the technique developed by Wilheit et al. (1991), which is then used to select profiles from the cloud model database used in the Bayesian retrieval

scheme (Kummerow et al. 2001). The TMI 2A12 freezing height is shown as a function of water vapor in Fig. 14a, along with the input Wilheit freezing-level estimate and the corresponding PR brightband height. Al-

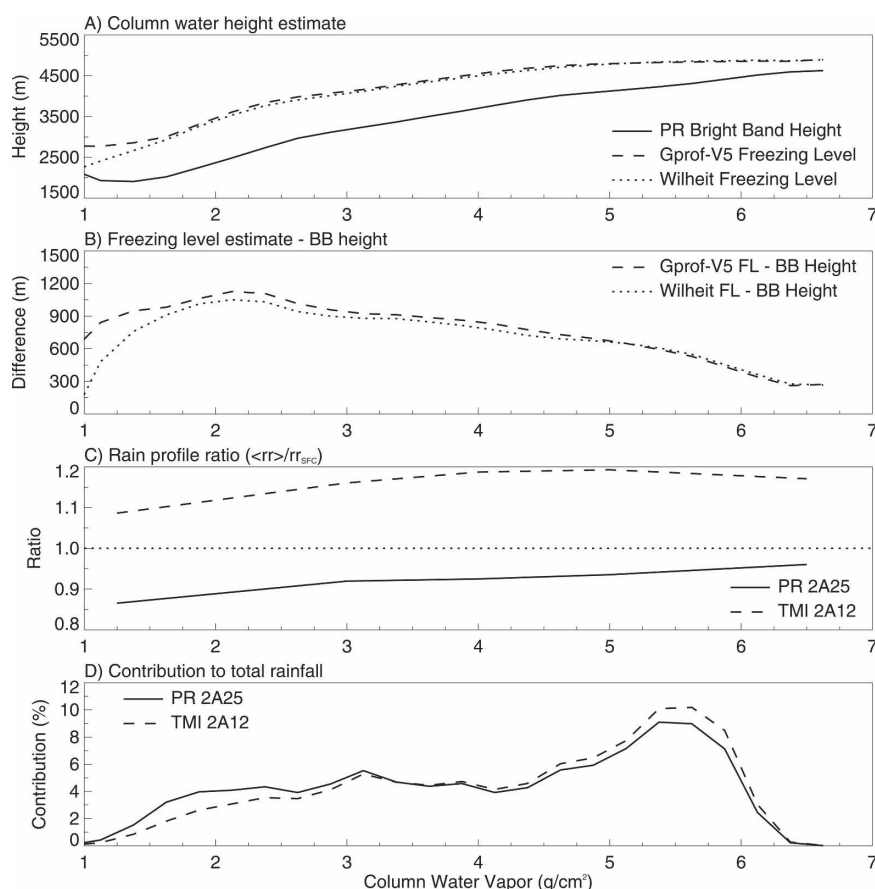


FIG. 14. Differences between 2A12 and 2A25 algorithm assumptions as a function of column water vapor. (a) The freezing height from the 2A12 algorithm and the 3A11 algorithm, along with the brightband height from the 2A25 algorithm. (b) The differences between the TMI freezing-level estimates and the PR brightband height. (c) The rain profile ratio for the 2A12 and 2A25 vertical profile retrievals, which is defined as the ratio of the mean rain rate between the surface and the bright band (determined from the PR) to the surface rain rate. (d) The rainfall contribution (%) for a given water vapor category for both the 2A12 and 2A25 retrievals.

though the freezing level is at the top of the melting layer and therefore above the bright band, differences between these two freezing-level estimates and the PR brightband height shown in Fig. 14b indicate substantial changes as a function of water vapor. The freezing-level estimates are within 300 m of the brightband height for high-water-vapor regions in the deep Tropics, but the mean difference increases to more than 1 km over the drier midlatitude regions. This result is consistent with previous studies by Harris et al. (2000) and Ikai and Nakamura (2003). Because an overestimate in the freezing level leads to a corresponding underestimate in the surface rainfall, this apparent high bias in the estimated freezing level over low-water-vapor regions may be largely responsible for the relative TMI rainfall deficiency over these dry areas depicted in Fig. 14d.

Changes in the shape of the rain profile as a function of column water vapor are indicated in Fig. 14c. The ratio of the vertically averaged rain rate between the surface and the PR bright band to the surface rain rate is computed to provide a simple measure of changes in the profile. While the TMI rain profiles contain consistently more water above the surface than do those of the PR, the dependence of a rain profile bias on water vapor is less apparent than in the freezing-level case. Clearly, further study into the impact of errors in these and other assumptions on the 2A12 algorithm is needed. As the examples shown in Fig. 14 indicate, however, evaluating errors in the algorithm assumptions as a function of column water vapor provides a way to investigate the global impact of errors in the algorithm assumptions that is independent of region and/or time.

6. Summary and discussion

The time-dependent nature of regional biases in the TRMM rainfall products means that these data may be inappropriate for some regional climate studies and/or investigations of climate variability. It also means that it is not possible to describe, and ultimately remove, these biases based on regionally defined characteristics. Instead, we have attempted to identify globally observable physical variables that can be used as a proxy for PR/TMI differences and, by association, the corresponding regime-dependent cloud properties. These proxy variables can then be used to identify, describe, and subsequently remove satellite rainfall biases using observations from field programs and/or complementary satellite sensors.

While climate rainfall biases resulting from differences in rainfall detection account for a relatively small

fraction of the total, the impact is substantial over certain regions. Given the inherently higher spatial resolution of the PR it is capable of detecting smaller, more isolated rain systems than the TMI, with its larger footprint. The frequency of occurrence of these isolated systems, however, exhibits significant regional variability, with the largest contribution coming from widespread isolated convection trailing midlatitude frontal systems during winter. The more challenging case to understand involves the detection of light rainfall by the TMI, which is not seen by the PR. This has a relatively small contribution to the total rainfall, with the exception of an area centered over the East China Sea. The frequent occurrence of rainfall detected by the TMI only in this region may to be linked to high-sulfate AODs. A hypothesis has been developed relating the presence of polluted air over this region to smaller cloud drops, which in turn allow for a significant increase in the amount of liquid water that the atmosphere can hold in the form of clouds before the onset of significant precipitation. Because the PR is relatively insensitive to clouds and light drizzle, this scenario provides a possible explanation for the absence of rain in the PR estimates associated with the high LWPs observed by the TMI. If true, this means that these TMI-only rain cases are either not precipitating or contain very light precipitation.

The bulk of the differences between the TMI and PR climate rainfall estimates are the result of differences in the estimated rain intensity. While previous studies have shown evidence relating these differences to changes in the assumptions used by the PR and TMI retrieval algorithms, temporal variations resulting from El Niño and the annual cycle make it impossible to export regional results from field studies. To address this issue over the entire TRMM ocean region we have identified total column water vapor as a proxy variable for TMI/PR differences. Accurate estimates of column water vapor are readily available over the global oceans from passive microwave sensors such as TMI for all but the most intense rainfall scenarios, in which case they can be interpolated from neighboring pixels. In addition, the relationship between column water and TMI/PR differences is very consistent from season to season and even between El Niño and La Niña. Categorizing the TMI/PR bias as a function of column water vapor and adjusting the TMI rain-rate estimates based on this relationship results in a consistent reduction of 65%–75% in the rms difference between PR and TMI climate rainfall estimates.

Because changes in algorithm assumptions can impact algorithms in very different ways, the goal of this

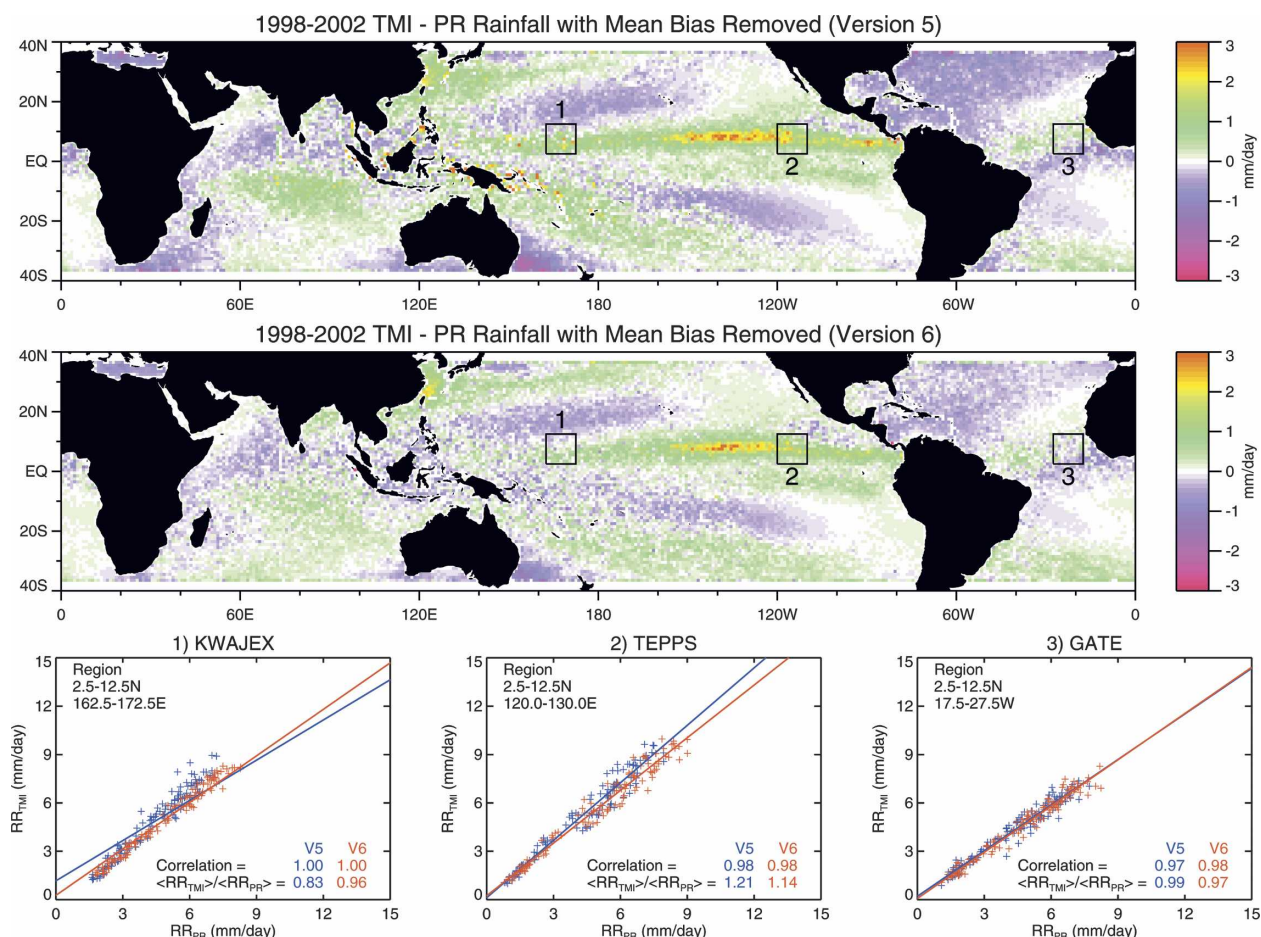


FIG. 15. Differences between TMI 2A12 and PR 2A25 rainfall averaged over the 5-yr period from 1998 through 2002 for (top) version 5 and (middle) version 6 of the retrieval algorithms. (bottom) Scatterplots of the rain estimates over $1^\circ \text{ lat} \times 1^\circ \text{ lon}$ boxes for the same three regions as shown in Fig. 2.

study has not been to identify how specific assumptions lead to climate biases in the TMI and PR retrievals, but to develop a mechanism to identify and subsequently correct for errors resulting from these systematic changes. As Fig. 15 shows, the changes between version 5 and the recently released version 6 of the TRMM algorithms have a significant impact on the regional and temporal differences between the two algorithms, although substantial regional differences remain. The value of a proxy variable is not necessarily the physical relationship between column water vapor and cloud properties (although that warrants further investigation), but the ability to characterize changes in the algorithm assumptions independent of location and time. In the case of the TMI 2A12 algorithm, examining the assumption of freezing-level height as a function of column water vapor reveals a substantial bias relative to the observed PR brightband height. This suggests that a freezing height correction based on column water vapor

may provide a means to remove a significant source of bias in the retrieval. Further examination of the impact of errors on the TMI and PR retrieval assumptions, such as the freezing level, is clearly needed. Categorizing changes in these assumptions in terms of the column water vapor, however, eliminates the need to characterize changes by region and/or time and provides a mechanism for exporting results from field programs and other in situ observations to other regions and/or seasons.

Acknowledgments. The authors thank Prof. Sonia Kreidenweis for her comments, Jody Thomas-Stahle for her assistance in modifying the 2A12 algorithm, and Brian Griffith for his assistance in computing LWP estimates over the East China Sea. Funding for this work was provided by the NASA TRMM program under Grant NAG5-13637. TMI Wentz products were produced by Remote Sensing Systems and sponsored

by the NASA Earth Science REASoN DISCOVER Project (www.remss.com). Aerosol data from the GOCART model were provided by Mian Chin at NASA's Goddard Space Flight Center.

REFERENCES

- Albrecht, B., 1989: Aerosols, cloud microphysics, and fractional cloudiness. *Science*, **245**, 1227–1230.
- Battaglia, A., C. Kummerow, D. Shin, and C. Williams, 2003: Constraining microwave brightness temperatures by radar brightband observations. *J. Atmos. Oceanic Technol.*, **20**, 856–871.
- Bauer, P., J. P. V. Póiares Baptista, and M. De Iulio, 1999: The effect of melting layer on the microwave emission of clouds over the ocean. *J. Atmos. Sci.*, **56**, 852–867.
- Bennartz, R., 1999: On the use of SSM/I measurements in coastal regions. *J. Atmos. Oceanic Technol.*, **16**, 417–431.
- Berg, W., C. Kummerow, and C. Morales, 2002: Differences between east and west Pacific rainfall systems. *J. Climate*, **15**, 3659–3672.
- Chen, S. S., R. A. Houze Jr., and B. E. Mapes, 1996: Multiscale variability of deep convection in relation to large-scale circulation in TOGA COARE. *J. Atmos. Sci.*, **53**, 1380–1409.
- Chin, M., R. B. Rood, S. Lin, J. Müller, and A. M. Thompson, 2000a: Atmospheric sulfur cycle simulated in the global model GOCART: Model description and global properties. *J. Geophys. Res.*, **105**, 24 671–24 687.
- , and Coauthors, 2000b: Atmospheric sulfur cycle simulated in the global model GOCART: Comparison with field observations and regional budgets. *J. Geophys. Res.*, **105**, 24 689–24 712.
- Del Genio, A. D., and W. Kovari, 2002: Climatic properties of tropical precipitating convection under varying environmental conditions. *J. Climate*, **15**, 2597–2615.
- DeMott, C. A., and S. A. Rutledge, 1998a: The vertical structure of TOGA COARE convection. Part I: Radar echo distributions. *J. Atmos. Sci.*, **55**, 2730–2747.
- , and —, 1998b: The vertical structure of TOGA COARE convection. Part II: Modulating influences and implications for diabatic heating. *J. Atmos. Sci.*, **55**, 2748–2762.
- Frisch, A. S., C. W. Fairall, and J. B. Snider, 1995: Measurement of stratus cloud and drizzle parameters in ASTEX with K_a -band Doppler radar and a microwave radiometer. *J. Atmos. Sci.*, **52**, 2788–2797.
- Fu, Y., and G. Liu, 2001: The variability of tropical precipitation profiles and its impact on microwave brightness temperatures and inferred from TRMM data. *J. Appl. Meteor.*, **40**, 2130–2143.
- Harris, G. N., Jr., K. P. Bowman, and D. Shin, 2000: Comparison of freezing-level altitudes from the NCEP reanalysis with TRMM precipitation radar brightband data. *J. Climate*, **13**, 4137–4148.
- Houze, R. A., Jr., S. S. Chen, D. E. Kingsmill, Y. Serra, and S. E. Yuter, 2000: Convection over the Pacific warm pool in relation to the atmospheric Kelvin–Rossby wave. *J. Atmos. Sci.*, **57**, 3058–3089.
- Iguchi, T., T. Kozu, R. Meneghini, J. Awaka, and K. Okamoto, 2000: Rain-profiling algorithm for the TRMM precipitation radar. *J. Appl. Meteor.*, **39**, 2038–2052.
- Ikai, J., and K. Nakamura, 2003: Comparison of rain rates over the ocean derived from TRMM Microwave Imager and precipitation radar. *J. Atmos. Oceanic Technol.*, **20**, 1709–1726.
- Ishizaka, Y., and Coauthors, 2003: The effect of air-pollutants on the microphysical properties of clouds over the sea off the southwest of Kyushu in Japan. Findings and current problems in the Asian Particle Environmental Change Studies: 2003, JST/CREST/APEX 2003 Interim Report, 103–116.
- Kummerow, C., W. Barnes, T. Kozu, J. Shiue, and J. Simpson, 1998: The Tropical Rainfall Measuring Mission (TRMM) sensor package. *J. Atmos. Oceanic Technol.*, **15**, 809–817.
- , and Coauthors, 2000: The status of the Tropical Rainfall Measuring Mission (TRMM) after two years in orbit. *J. Appl. Meteor.*, **39**, 1965–1982.
- , and Coauthors, 2001: The evolution of the Goddard profiling algorithm (GPROF) for rainfall estimation from passive microwave sensors. *J. Appl. Meteor.*, **40**, 1801–1820.
- , P. Poyner, W. Berg, and J. Thomas-Stahle, 2004: The effects of rainfall inhomogeneity on climate variability of rainfall estimated from passive microwave sensors. *J. Atmos. Oceanic Technol.*, **21**, 624–638.
- Liu, Y., and P. Daum, 2004: On the parameterization of the autoconversion process. Part I: Analytical formulation of the Kessler-type parameterizations. *J. Atmos. Sci.*, **61**, 1539–1548.
- , —, and R. McGraw, 2004: An analytical expression for predicting the critical radius in autoconversion parameterization. *Geophys. Res. Lett.*, **31**, L06121, doi:10.1029/2003GL019117.
- Marshall, J. S., and W. M. Palmer, 1948: The distribution of raindrops with size. *J. Meteor.*, **5**, 165–166.
- Masunaga, H., T. Iguchi, R. Oki, and M. Kachi, 2002: Comparison of rainfall products derived from TRMM Microwave Imager and precipitation radar. *J. Appl. Meteor.*, **41**, 849–862.
- , T. S. L'Ecuyer, and C. D. Kummerow, 2005: Variability in the characteristics of precipitation systems in the tropical Pacific. Part I: Spatial structure. *J. Climate*, **18**, 823–840.
- Miles, L. M., J. Verlinde, and E. E. Clothiaux, 2000: Cloud droplet size distributions in low-level stratiform clouds. *J. Atmos. Sci.*, **57**, 295–311.
- Nesbitt, S. W., E. J. Zipser, and D. J. Cecil, 2000: A census of precipitation features in the tropics using TRMM: Radar, ice scattering, and lightning observations. *J. Climate*, **13**, 4087–4106.
- , —, and C. D. Kummerow, 2004: An examination of version-5 rainfall estimates from the TRMM Microwave Imager, precipitation radar, and rain gauges on global, regional, and storm scales. *J. Appl. Meteor.*, **43**, 1016–1036.
- Olson, W. S., P. Bauer, C. D. Kummerow, Y. Hong, and W. Tao, 2001: A melting-layer model for passive/active microwave remote sensing applications. Part II: Simulation of TRMM observations. *J. Appl. Meteor.*, **40**, 1164–1179.
- Petersen, W. A., and S. A. Rutledge, 2001: Regional variability in tropical convection: Observations from TRMM. *J. Climate*, **14**, 3566–3586.
- , S. W. Nesbitt, R. J. Blakeslee, R. Cifelli, P. Hein, and S. A. Rutledge, 2002: TRMM observations of intraseasonal variability in convective regimes over the Amazon. *J. Climate*, **15**, 1278–1294.
- , R. Cifelli, D. J. Boccippio, S. A. Rutledge, and C. Fairall, 2003: Convection and easterly wave structures observed in the eastern Pacific warm pool during EPIC-2001. *J. Atmos. Sci.*, **60**, 1754–1773.
- Petty, G. W., 1995: Frequencies and characteristics of global oce-

- anic precipitation from shipboard present-weather reports. *Bull. Amer. Meteor. Soc.*, **76**, 1593–1616.
- , 1997: An intercomparison of oceanic precipitation frequencies from 10 special sensor microwave/imager rain rate algorithms and shipboard present weather reports. *J. Geophys. Res.*, **102**, 1757–1777.
- Rickenbach, T. M., and S. A. Rutledge, 1998: Convection in TOGA COARE: Horizontal scale, morphology, and rainfall production. *J. Atmos. Sci.*, **55**, 2715–2729.
- Robertson, F. R., D. E. Fitzjarrald, and C. D. Kummerow, 2003: Effects of uncertainty in TRMM precipitation radar path integrated attenuation on interannual variations of tropical oceanic rainfall. *Geophys. Res. Lett.*, **30**, 1180, doi:10.1029/2002GL016416.
- Schumacher, C., and R. A. Houze Jr., 2000: Comparison of radar data from the TRMM satellite and Kwajalein oceanic validation site. *J. Appl. Meteor.*, **39**, 2151–2164.
- Stephens, G. L., and Coauthors, 2002: The CloudSat mission and the A-train. *Bull. Amer. Meteor. Soc.*, **83**, 1771–1790.
- Wentz, F. J., and R. W. Spencer, 1998: SSM/I retrievals within a unified all-weather ocean algorithm. *J. Atmos. Sci.*, **55**, 1613–1627.
- , C. Gentemann, D. Smith, and D. Chelton, 2000: Satellite measurements of sea surface temperatures through clouds. *Science*, **288**, 847–850.
- Wilheit, T. T., A. T. C. Chang, and L. S. Chiu, 1991: Retrieval of monthly rainfall indices from microwave radiometric measurements using probability distribution functions. *J. Atmos. Oceanic Technol.*, **8**, 118–136.